# Simulation and Precipitation Detection in the Tropical Cyclones Based on the Microwave Humidity and Temperature Sounder Onboard the Fengyun-3C Satellite

**Na Li[1, 2, *], Shengwei Zhang[1], and Jieying He[1]**

**Abstract**—Tropical cyclone (TC) is part of the most serious natural disasters. Western Pacific is the region with the highest frequency of tropical cyclones (TCs). By simulating and correcting the brightness temperatures (TBs) of the microwave humidity and temperature sounder (MWHTS) onboard the Fengyun-3C (FY-3C) satellite, a method is proposed to observe the TCs in the Western Pacific. The Weather Research and Forecasting Model (WRF) and the fast Radiative Transfer model for TOVS (RTTOV) are adopted in our method. Then, simulated TBs are linearly corrected based on the field-of-views (FOVs), channels and latitude bands. After that, the biases of all channels are within 2 K and close to zero, and the RMSEs are less than 10-K except Channels 10 and 15. Therefore, this WRF/RTTOV method can be implemented in other TCs in the Western Pacific region. In addition, a precipitation detection algorithm is proposed and used to detect precipitation in the TC area. Compared with the FY-3C MWHTS and Tropical Rainfall Measuring Mission (TRMM) Multi-Satellite Precipitation Analysis (TMPA) precipitation products, the results indicate that our precipitation detection algorithm has reached better indicators. The potential application can lay a foundation for precipitation rate retrieval and further research.

## 1. INTRODUCTION

A tropical cyclone (TC) is a rapidly rotating storm system characterized by a low-pressure center, closed low-level atmospheric circulation, strong wind, and spiral arrangement of thunderstorms that produce heavy rain [1]. It influences human life, property and their activities seriously. Nevertheless, the damage could be reduced by effective preparation, as long as TCs are predictable [2]. Therefore, it is extremely important to study the process of its occurrence, development, and demise. The Western Pacific is the region where TCs occur most frequently in the world. It is of profound significance to conduct simulation studies on the TCs area.

Satellite-based remote sensing is a traditional method to observe TCs. In recent years, research on TCs with satellites in geosynchronous orbit has been developed rapidly with many achievements. For example, Zhang et al. [3, 4] used near real case observation modeled by WRF/RTTOV method in the geostationary interferometer microwave sounder (GIMS) to simulate TC. Camps et al. [5] presented the generic architecture of Synthetic Aperture Interferometric Radiometer Performance Simulator (SAIRPS). They not only completed the algorithms in the Radiative Transfer Module, but also analyzed and simulated the results to show its performance. Compared to satellites in geosynchronous orbit, polar orbiting satellites have superior resolution for observing the earth surface due to their lower orbital altitude. However, polar orbiting satellites cannot continuously observe the same area, making it

difficult to observe the rapid changes of the TCs continuously. In order to address the problem described above, a method is proposed to simulate the TBs from the microwave humidity and temperature sounder (MWHTS) onboard the Fengyun-3C (FY-3C) satellite. Then, as an application, precipitation detection algorithm is suggested to detect precipitation in TCs area.

This paper is structured as follows. Section 2 shows the FY-3C MWHTS and its data. Section 3 describes the experiments, including the study area and experiments in design. The correction algorithm and precipitation detection algorithm are also introduced in this section. Section 4 presents the results and discussion, involving the consequences of corrected TBs and precipitation detection. A summary is described in Section 5.

## 2. FY-3C AND MWHTS

The Fengyun-3C (FY-3C) polar orbiting meteorological satellite is the third satellite of the second generation polar-orbit meteorological satellite, which was launched in China on September 23, 2013. It passes over the equator between 10:00 a.m. and 10:20 a.m. (local time). The microwave humidity and temperature sounder (MWHTS) [6–8] onboard the FY-3C satellite is a total power millimeter microwave radiometer working in cross-track scanning mode with 15 channels. The operating frequency of the MWHTS includes 89 GHz, 118.75 GHz, 150 GHz, and 183.31 GHz. Channels' characteristics of the MWHTS receivers can be found in Table 1. These 15 channels' weighting functions are shown in Figure 1, and the weighting functions for each channel are calculated from U.S. standard atmosphere climatology with the Community Radiative Transfer Model (CRTM) [9–11]. There are 13 horizontal polarized channels in total. In detail, 8 and 5 detection channels are designed near the 118.75 GHz oxygen resonance line and the 183.31 GHz water vapor resonance line, respectively. Especially, 118.75-GHz is firstly used in the polar orbit meteorological satellite. The combined detection of 118.75-GHz and 183.31-GHz makes it possible to detect the temperature profiles and humidity profiles in the vertical direction simultaneously. In addition, vertical polarization channels are designed for 89 GHz and 150 GHz. These two transparent channels (also called window channels) are sensitive to the ground surface and can observe the precipitation in TCs area.

Temporal coverage for available FY-3C MWHTS data is from 30 September 2013 to present. The

**Table 1.** FY-3C MWHTS channels information.

| No. | Center frequency (GHz) | Polari zation[1] | Band Width (MHz) | LO Precision (MHz) | Dynamic Range (K) | Sensitivity NEΔT (K) | Calibration accuracy (K) | 3 dB Beam Width |
|-----|------------------------|------------------|------------------|--------------------|-------------------|----------------------|--------------------------|-----------------|
| 1 | 89.0 | V | 1500 | 50 | 3–340 | 1.0 | 1.3 | 2.0° |
| 2 | 118.75 ± 0.08 | H | 20 | 30 | 3–340 | 3.6 | 2.0 | 2.0° |
| 3 | 118.75 ± 0.2 | H | 100 | 30 | 3–340 | 2.0 | 2.0 | 2.0° |
| 4 | 118.75 ± 0.3 | H | 165 | 30 | 3–340 | 1.6 | 2.0 | 2.0° |
| 5 | 118.75 ± 0.8 | H | 200 | 30 | 3–340 | 1.6 | 2.0 | 2.0° |
| 6 | 118.75 ± 1.1 | H | 200 | 30 | 3–340 | 1.6 | 2.0 | 2.0° |
| 7 | 118.75 ± 2.5 | H | 200 | 30 | 3–340 | 1.6 | 2.0 | 2.0° |
| 8 | 118.75 ± 3.0 | H | 1000 | 30 | 3–340 | 1.0 | 2.0 | 2.0° |
| 9 | 118.75 ± 5.0 | H | 2000 | 30 | 3–340 | 1.0 | 2.0 | 2.0° |
| 10 | 150.0 | V | 1500 | 50 | 3–340 | 1.0 | 1.3 | 1.1° |
| 11 | 183.31 ± 1 | H | 500 | 30 | 3–340 | 1.0 | 1.3 | 1.1° |
| 12 | 183.31 ± 1.8 | H | 700 | 30 | 3–340 | 1.0 | 1.3 | 1.1° |
| 13 | 183.31 ± 3 | H | 1000 | 30 | 3–340 | 1.0 | 1.3 | 1.1° |
| 14 | 183.31 ± 4.5 | H | 2000 | 30 | 3–340 | 1.0 | 1.3 | 1.1° |
| 15 | 183.31 ± 7 | H | 2000 | 30 | 3–340 | 1.0 | 1.3 | 1.1° |

[1] Note: In column 3, $V/H$ means quasi $V/H$ polarization.
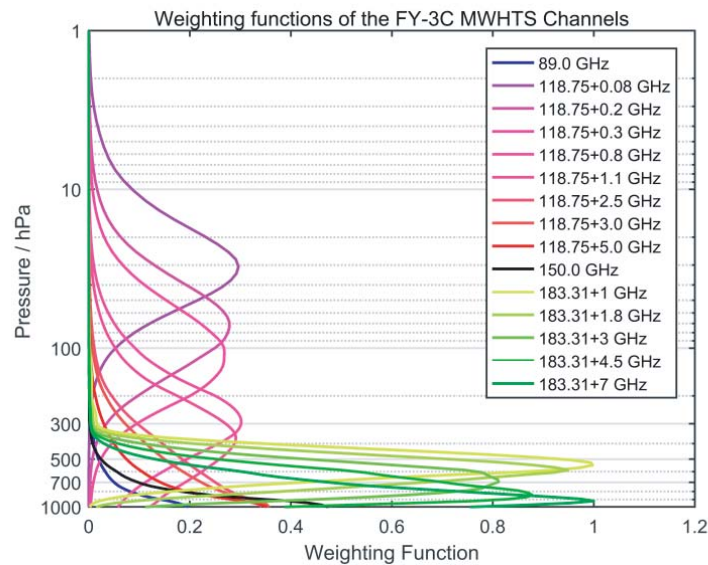
**Figure 1.** Weighting functions for 15 channels of FY-3C MWHTS.

microwave radiometer sounder [6–8] provides dual polarization observations (vertical and horizontal polarization) at frequencies ranging from 89 to 183.31-GHz. The integrated field of views (FOVs, 3-dB footprint size) range from $15 \times 15$-km to $27 \times 41$-km. The microwave sounder contains Level 1 (L1) and Level 2 (L2) data, which are shown on the website: http://satellite.nsmc.org.cn/portalsite/default.aspx. They are both orbit data and are recorded every 102 minutes for one orbit of the FY-3C. These two datasets are recorded with same temporal and spatial resolution. In detail, the Level 1 data contain time, latitude, longitude, brightness temperatures (TBs), sensor zenith angle, the mask of land and ocean, etc. In this paper, the Level 1 data are used to correct and evaluate the simulated TBs. The Level 2 (L2) data are a precipitation detection product that contains information about rain detection, surface type, scattering index, etc. They are used to evaluate and analyze the validation of precipitation detection algorithm.

## 3. EXPERIMENTS

### 3.1. Study Area

TCs occurs frequently every year. About 80 to 100 TCs occur each year in the global tropical oceans. In detail, about 32% of them are present in the Western Pacific Ocean, which is the most typhoon-producing region in the world [12]. Therefore, the Western Pacific Ocean is the region where TCs occur most frequently. In this paper, 16 TCs [13] in the Western Pacific Ocean between 2015 and 2017 are simulated and analyzed. Table 2 shows some information about these sixteen typhoons. The study area and cumulative tracks of these TCs are presented in Figure 2. Among them, the No. 17 typhoon MEGI is used to verify the brightness temperatures simulation experiment and precipitation detection algorithm, and other typhoons are utilized to build the experiment and algorithm.

### 3.2. Experiments Design

The final operational global analysis data of the National Centers for Environmental Prediction (NCEP) [14, 15] are utilized to initialize the WRF Preprocessing System (WPS) and Weather Research and Forecasting (WRF) [16–18] models in this paper. These two models will generate atmospheric profiles and surface parameters at a certain time difference. In detail, atmospheric profile parameters include temperature, humidity, cloud fraction and hydrometeor content profile. The atmospheric surface parameters include u- and v-winds at 10-m, surface skin temperature, surface emissivity, land mask,
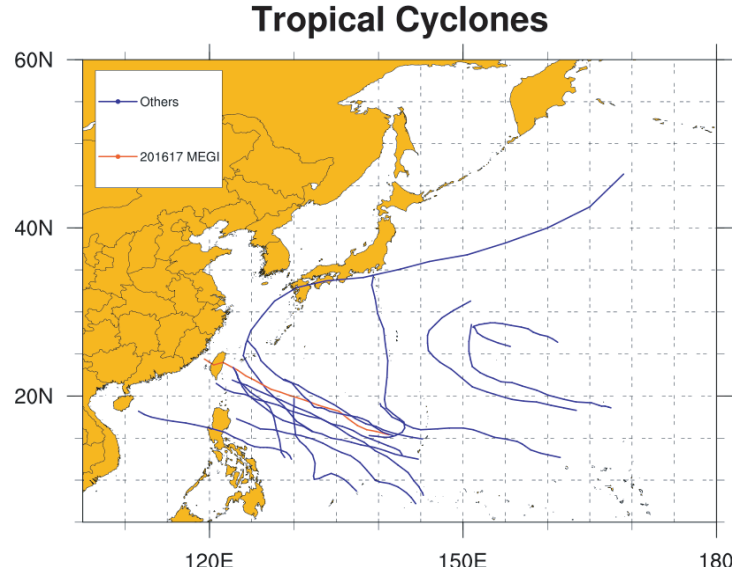
## Tropical Cyclones



**Figure 2.** The cumulative tracks of the TCs studied during 2015–2017.

**Table 2.** The three TCs parameter set by WRF simulation.

| No. | TCs Name | Time | Latitude (°N) | Longitude (°E) | Grid Points (horizontal) | Amount of data |
|---|---|---|---|---|---|---|
| 1 | 201521 Dujuan | 2015.9.22–2015.9.29 | 15.2–27.7 | 114.8140.2 | 123 × 66 | 135,461 |
| 2 | 201523 ChoiWan | 2015.10.2–2015.10.8 | 15.7–40.9 | 145.4–168.2 | 111 × 141 | 188,996 |
| 3 | 201525 Champi | 2015.10.13–2015.10.25 | 12.7–33.0 | 134.8–160.2 | 123 × 108 | 373,048 |
| 4 | 201601 Nepartak | 2016.7.3–2016.7.10 | 8.1–26.3 | 114.8145.2 | 147 × 93 | 302,672 |
| 5 | 201609 MINDULLE | 2016.8.19–2016.8.22 | 15.0–34.0 | 137.9–143.3 | 27 × 102 | 25,271 |
| 6 | 201614 MERANTI | 2016.9.10–2016.9.15 | 15.0–25.8 | 116.7–14.2 | 114 × 57 | 87,344 |
| 7 | 201616 MALAKAS | 2016.9.12–2016.9.19 | 1.2–29.8 | 119.8140.2 | 99 × 102 | 182,247 |
| 8 | 201617 MEGI | 2016.9.23–2016.9.29 | 13.1–28.5 | 113.0–143.3 | 147 × 81 | 186,691 |
| 9 | 201620 SONGDA | 2016.10.8–2016.10.13 | 18.2–38.1 | 143.0–165.2 | 108 × 111 | 122,350 |
| 10 | 201621 SARIKA 201622 HAIMA | 2016.10.13–2016.10.21 | 5.2–24.8 | 105.5–145.2 | 192 × 99 | 468,652 |
| 11 | 201703 NANMADOL | 2017.7.2–2017.7.4 | 16.9–32.0 | 120.0–135.4 | 75 × 81 | 33,546 |
| 12 | 201705 NORU | 2017.7.21–2017.8.1 | 19.8–32.0 | 134.8–160.2 | 123 × 66 | 210,343 |
| 13 | 201709 NESAT | 2017.7.25–2017.7.29 | 13.8–24.2 | 120.0–132.3 | 60 × 54 | 36,694 |
| 14 | 201718 TALIM | 2017.9.9–2017.9.17 | 15.1–30.0 | 119.8145.2 | 123 × 78 | 177,733 |
| 15 | 201721 LAN | 2017.10.15–2017.10.22 | 8.2–31.8 | 117.9138.3 | 51 × 123 | 124,406 |

temperature and vapor at 2-m. Then, the atmospheric profiles and surface parameters are used as the input atmospheric parameters of the fast Radiative Transfer model for TOVS (RTTOV) [19, 20] developed by European Center for Medium-Range Weather Forecasts (ECMWF) to simulate the TBs of the FY-3C MWHTS. After that, simulated TBs are generated as the simulation outputs. The simulation outputs are linearly corrected to get closer to the observed TBs from the FY-3C MWHTS sensor. Finally, a precipitation detection algorithm is suggested to detect precipitation in TCs area. The simulation framework of TCs is illustrated in Figure 3.

The details of the TCs are shown in Table 2. They have different horizontal resolutions and the same vertical resolution. The horizontal resolutions of these three TCs between the adjacent grid points
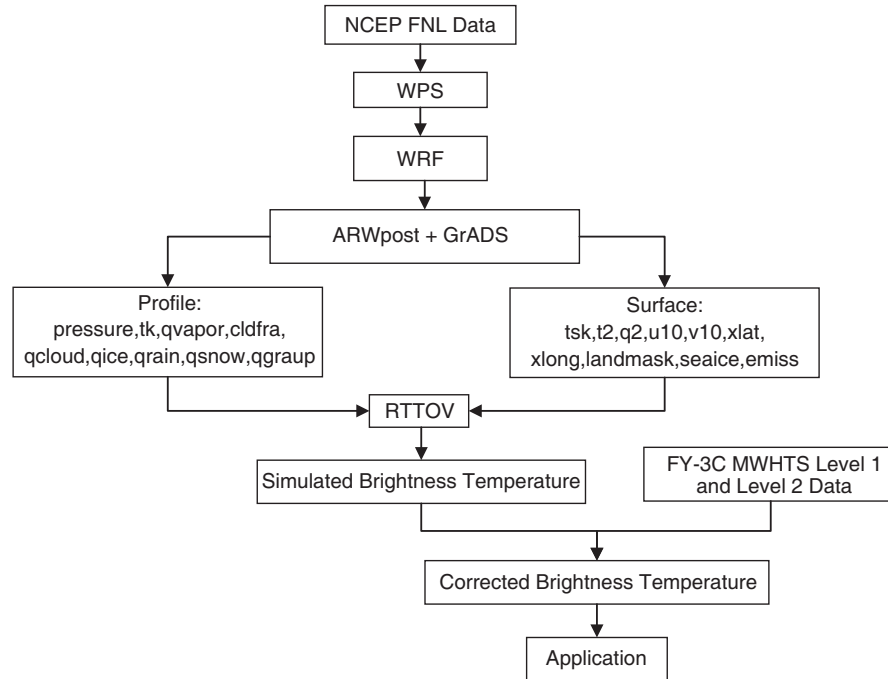
**Figure 3.** Framework of TCs simulation for the FY-3C MWHTS.

are all 20 km approximately. Detailed grid points of these three TCs are $123 \times 66$, $147 \times 93$, $147 \times 81$ along longitude and latitude, respectively. The vertical direction is divided into 29 levels.

In summary, WRF + RTTOV models are run for some days around TCs after being initialized with the NCEP analysis. The output is subsequently compared with the observed TBs from the MWHTS sensor, and the simulation outputs are linearly corrected to get closer to the observations. The structure of the TC can be obviously observed in the map drawn from the simulated TBs. However, due to the limitations of the water particle scattering module and the surface emission module of the fast radiation transmission model RTTOV, there are always errors in the simulation of the TC area. In order to better apply the simulated TBs, it is necessary to correct the simulated TBs before applying them. Therefore, we develop a correction method, representing the linear relationship between the simulated and observed TBs. In addition, a precipitation detection algorithm is suggested in this paper.

### 3.2.1. Models — WRF and RTTOV

The Weather Research and Forecasting (WRF) Model [16–18] is a mesoscale numerical weather prediction system jointly developed by scientific organizations such as the National Center for Atmospheric Research (NCAR) and the National Oceanic and Atmospheric Administration (represented by the National Centers for Environmental Prediction (NCEP). This model is intended for hurricane research, data assimilation research, operational forecasting applications and other atmospheric researches. Additionally, it is appropriate to use in a broad range of applications across scales ranging from meters to thousands of kilometers. In this paper, the NCEP final operational global analysis data prepared operationally every 6 hours are adopted in order to initialize the WRF model. The WRF model offers multiple schemes for every physical component. The microphysical process is a WRF single-moment 6-class microphysics scheme (WSM6) [21] with water vapor, cloud water, ice, rain, snow, graupel as the six predictive variables. WSM6 is a mature microphysical scheme and has been used widely. Other schemes, such as the Kain-Fritsch scheme [22], Dudhia scheme [23], Rapid radiative transfer model (RRTM) [24], MM5 Monin-Obukhov scheme, Noah land surface model [25, 26], and YonSei University scheme (YSU) [27] are applied in this study. In detail, physical parameterizations schemes [28] adopted by the WRF simulation are presented in Table 3.

The fast Radiative Transfer model for TOVS (RTTOV) [19, 20] is originally developed at ECMWF

**Table 3.** The physical parameterizations schemes used by WRF simulation.

| Physical process | Options |
|---|---|
| Microphysical process | The WRF single-moment 6-class microphysics scheme [21] |
| Cumulus Convection Parameterization | Kain-Fritsch scheme [22] |
| Short wave radiation process | Dudhia scheme [23] |
| Long wave radiation process | Rapid radiative transfer model (RRTM) [24] |
| Surface process | MM5 Monin-Obukhov scheme |
| Land process | Noah land surface Model [25, 26] |
| Planetary boundary layer scheme | The YonSei University scheme (YSU) [27] |

in the early 90's for TOVS. It is designed to simulate satellite radiance for passive visible, infrared and microwave downward-viewing satellite radiometers, spectrometers and interferometers. In microwave the frequency range is from 10 to 800 GHz which is covered using the Liebe-89 MPM line-by-line model. In addition to the clear sky condition, RTTOV can provide simulation of microwave radiance affected by cloud and precipitation. In cloudy and rainy weather, the atmosphere contains a large number of hydrometeors particles, which cause a strong scattering effect. In the RTTOV model, delta-Eddington approximation is utilized to compute the scattering effects of hydrometeors at microwave frequencies. Therefore, RTTOV computes the radiance in the clear air part but adds the scattering effects from water/ice in the profile, and it uses a two-independent column approximation. The total brightness temperature $T_B^{\text{Total}}$ can be written as:

$$T_B^{\text{Total}} = (1 - C)T_B^{\text{Clear}} + CT_B^{\text{Rainy}} \tag{1}$$

where $C$ is the effective cloud fraction in the vertical profile, and $T$ is the brightness temperature. In detail, $T_B^{\text{Clear}}$ is the brightness temperature in the clear sky, and $T_B^{\text{Rainy}}$ is the brightness temperature from the scattering effects of hydrometeors particles. The optical parameters of the hydrometeors particles (cloud liquid water, cloud ice water, water vapor, rain and snow) are obtained by lookup tables for Mie scattering properties. Finally, Equation (1) is used to linearly combine the twoindependent columns, producing the total brightness temperature $T_B^{\text{Total}}$.

*3.2.2. Correction*

In simulating the TBs of tropical cyclones, simulated TBs can be affected by many factors, resulting in an error between the simulated TBs and the observed TBs. TCs are an integral part of the atmospheric cycle, passing heat from the equatorial region to high latitudes. During the movement of TCs from low latitude to high latitude, energy is gradually reduced. Therefore, different latitudes have a greater impact on the TBs simulation. Moreover, when the sensor is performing linear scanning, the detection points at the edge of the scanning line are seriously tilted due to the detection angle, and the atmospheric radiation path between the sounding channels and the scanning points (also known as field-of-views FOVs) at the edge is longer than the atmospheric radiation path between the sounding channels and sub-satellite points. The amount of received radiation is reduced, and it is easy to form edge effects, which can lead to errors in the simulation.

In addition to edge effects and latitude differences, sounding channels set at different frequencies also have different errors in the simulation. Taking these three aspects into consideration, in this paper, the simulated TBs are linearly corrected [29] based on the different classes of 98 field-of-views (FOV), 15 channels, and 7 latitude bands (5°N–10°N, 10°N–15°N, 15°N–20°N, 20°N–25°N, 25°N–30°N, 30°N–35°N and 35°N–40°N). That is to say, this paper is divided into $98 \times 15 \times 7 = 10,290$ categories to correct the simulated TBs. This procedure calculates $10,290 \times 3 = 30,870$ coefficients (the $a_{ijk}$, $b_{ijk}$ and $c_{ijk}$ of Equation (2)), obtained by fitting the residuals (corrected minus observed) with the least square method. The correction equation is shown in Equation (2). In addition, except for the No. 17 typhoon MEGI to verify Equation (2), the other 15 typhoons in Table 2 are utilized to calculate these

coefficients (the $a_{ijk}$, $b_{ijk}$ and $c_{ijk}$ of Equation (2)) and establish Equation (2).

$$TB_{ijk}^* = a_{ijk}TB_{ijk} + b_{ijk}\beta + c_{ijk} \tag{2}$$

where $TB_{ijk}^*$ represents the corrected TBs; $TB_{ijk}$ represents the simulated TBs; $\beta$ is the sensor zenith angle of the FY-3C MWHTS; $a_{ijk}$, $b_{ijk}$ and $c_{ijk}$ are the correction coefficients; $i$ is the channels number (1–15); $j$ is the FOVs number (1–98); $k$ is the latitude bands ($k = 7$).

### 3.2.3. Precipitation Detection Algorithm

The window channels are equipped with a certain degree of transparency and can be used to observe the earth surface. The window channels of the FY-3C MWHTS are designed as the vertical polarization channels at 89 GHz and 150 GHz. They are sensitive to the water vapor absorption over the ocean and the hydrometeor scattering [30] and contain the humidity information. Therefore, they are useful for observing the precipitation and structure of TCs.

According to the algorithm of [31, 32], this paper proposes the scattering index for the FY-3C MWHTS and further proposes the precipitation detection algorithm for TCs occurring in the Western Pacific Ocean.

Based on the TBs from the 89-GHz and 150-GHz window channels, the scattering index ($SI$) is defined in Equation (3).

$$SI = (TB_{89} - TB_{150}) - (a_1 + a_2\beta) \tag{3}$$

where $SI$ represents the scattering index; $TB_{89}$ and $TB_{150}$ represent the corrected TBs of the 89-GHz and 150-GHz channels, respectively; $\beta$ is the sensor zenith angle; $a_1$ and $a_2$ represent the regression coefficients.

Determining scattering index thresholds ($SI_0$) is the key to detecting precipitation in TCs area. In this paper, the threshold $SI_0$ is determined by both the $SI$ calculated by Equation (3) and precipitation detection from the FY-3C MWHTS Level 2 data. Then, $SI_0$ is used to detect the precipitation. In detail, when $SI$ calculated by Equation (3) is greater than $SI_0$, the observed area is considered as precipitation. On the contrary, when the $SI$ is less than $SI_0$, the observed area is considered as no precipitation.

This algorithm is validated with the Probability of Detection (POD), False Alarm Ratio (FAR) and Critical Success Index (CSI) [33–35] in this paper. These three metrics are shown in Table 4. The POD is an index of correct detection. The FAR is an index of false rainfall, and the CSI is an index of correct detection considering false alarms. These three metrics are used to validate and evaluate the precipitation detection algorithm. Among them, the closer the FAR is to 0%, and the closer the POD and the CSI are to 100%, the better the precipitation detection algorithm is.

**Table 4.** List of the statistical metrics used in the evaluation and comparison[1].

| Statistical Index | FY3C MWHTS L2 | Perfect Value |
|---|---|---|
| Probability of Detection (POD) | $POD = \frac{N_{11}+N_{00}}{N_{11}+N_{00}+N_{01}} \times 100\%$ | 100% |
| False Alarm Ratio (FAR) | $FAR = \frac{N_{10}}{N_{11}+N_{00}+N_{10}} \times 100\%$ | 0% |
| Critical Success Index (CSI) | $CSI = \frac{N_{11}+N_{00}}{N_{11}+N_{00}+N_{10}+N_{01}} \times 100\%$ | 100% |

[1] Note: $N$ represents the number of samples; $N_{11}$ represents the hits with precipitation; $N_{00}$ represents the hits with non-precipitation; $N_{10}$ represents the false alarms with non-precipitation; $N_{01}$ is contrary to $N_{10}$, namely, it represents the misses when precipitation.

## 4. RESULTS AND DISCUSSION

In this paper, 16 TCs of the Western Pacific shown in Table 2 are used to study. In detail, the No. 17 typhoon MEGI is utilized to verify the TBs simulation experiment, the corrected coefficients in

Equation (2) and precipitation detection algorithm, and the others are used to build the TBs simulation experiment and precipitation detection algorithm.

## 4.1.  Correction

Mean biases of the simulated TB errors for MWHTS Channels 1–15 against the observed TBs are shown in Figure 4, and Figure 5 is the mean of the corrected TB errors. Mean biases between simulated TBs and observed TBs in Channels 1–9 and 11–14 (except the first few FOVs in Channels 12–14) before bias correction are large, but are within 2 K and close to zero after bias correction. This indicates that the correction algorithm proposed in this paper is effective and feasible for simulating the TBs in TCs area.
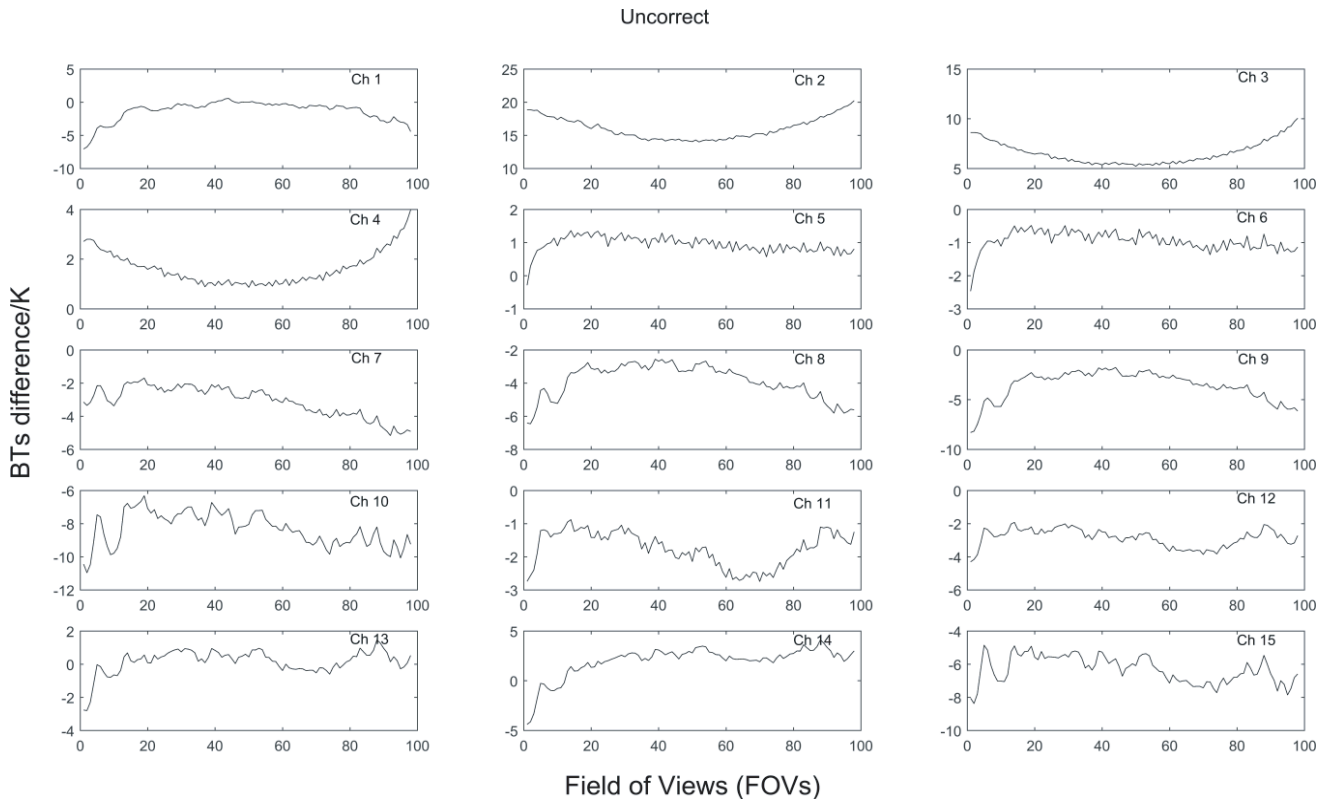


**Figure 4.** Difference of observed BTs for MWHTS Channels (Ch 1–15) against the simulated BTs.

However, Channels 10 and 15 have big biases after the bias correction.  There are some reasons for this result.  Typhoon originates in the tropical sea, where the temperature is high, and a large amount of seawater is evaporated into the air to form a low-pressure center. Therefore, the typhoon is closely linked to the sea surface and the atmosphere close to the surface, where it can be observed by Channels 10 and 15, and the surface emissivity over ocean is calculated by the FASTEM-5 module in the RTTOV radiation transmission model. Although the surface emissivity of the calm sea is stable and calculated accurately, the sea where the typhoon is located is rough, and this will bring a vast error to the calculation of the typhoon sea surface emissivity. In addition, typhoons are usually accompanied by precipitation, resulting in a significant increase in the number of ice water particles in the atmosphere and Earth's surface, which will increase the scattering effect. Nevertheless, the scattering module in the RTTOV model is not as accurate as the clear sky module.

In order to quantitatively evaluate the performance of the bias correction method further, the biases and root-mean-square errors (RMSE) for 15 channels are used. The errors of pre-correction and post-correction are given in Figure 6.  It can be seen that the bias without bias correction is large,
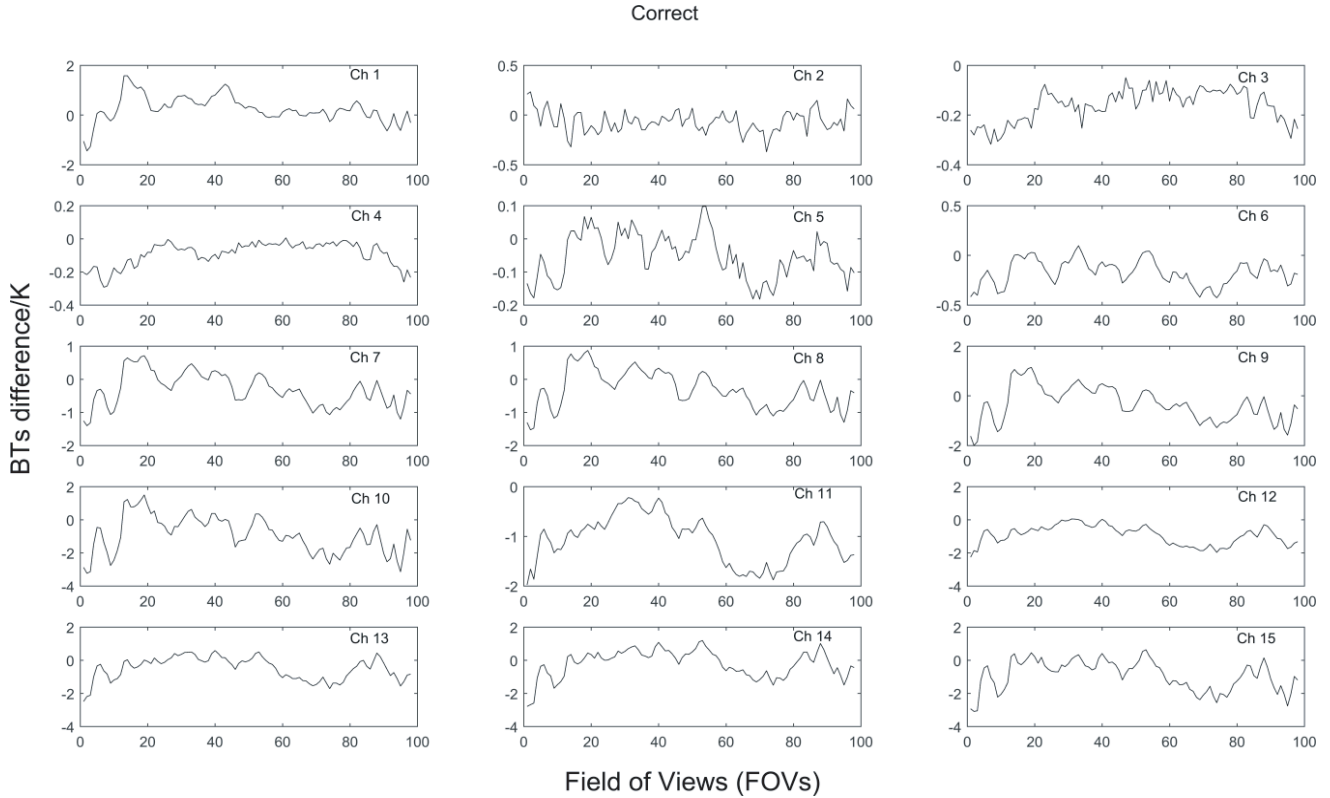
**Figure 5.** Difference of observed BTs for MWHTS Channels (Ch 1–15) against the corrected BTs.
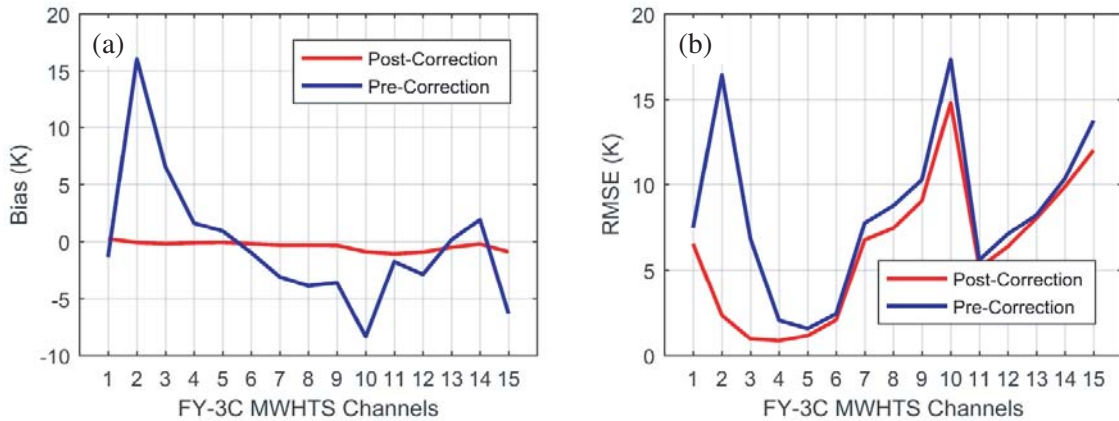


**Figure 6.** Pre-correction and post-correction errors. (a) Bias; (b) RMSE.

especially in Channels 2, 10 and 14–15. Among them, Channels 10 and 14–15 are vulnerable to the Earth's surface and the atmosphere close to the surface. However, the biases for all channels are smaller and close to zeros after the bias correction. In addition, the RMSEs of the five channels 2, 9, 10, 14 and 15 are all greater than 10 K before the correction. However, after the correction, the biases of all channels are close to 0-K, and the RMSEs of all channels are less than 10-K except Channels 10 and 15. Above all, the corrected TBs have less bias than the uncorrected TBs (simulated TBs) for all channels. Although the RMSE has also been reduced for all channels, it is not improved obviously. The results show that our correction algorithm for the simulated TBs is feasible.

Although the accuracies of corrected TBs in Channels 10 and 15 are lower than other channels, and

the result of the correction error is not as effective as other channels, the deviation does not exceed 3.5 K. In all, the mean biases in all channels have been significantly reduced after bias correction. Therefore, the correction method can be effectively corrected and get the desired correction consequences. At the same time, the results show that in the process of correcting the simulated TBs, considering these three influencing factors of the edge effect, different latitude bands and channels are reasonable and scientific.

In this paper, the NCEP FNL/WRF/RTTOV method is adopted to simulate and correct the TBs, then the corrected TBs are used to draw some TBs maps. As an application, the window channels 1 and 10 are utilized to detect precipitation in the TCs area. Figure 7 shows the TBs maps with the simulated, corrected and observed TBs for these two window channels. As this experiment results, we can not only observe and evaluate the simulated and observed TBs in this paper, but also make an evaluation of the performance of the correction method.
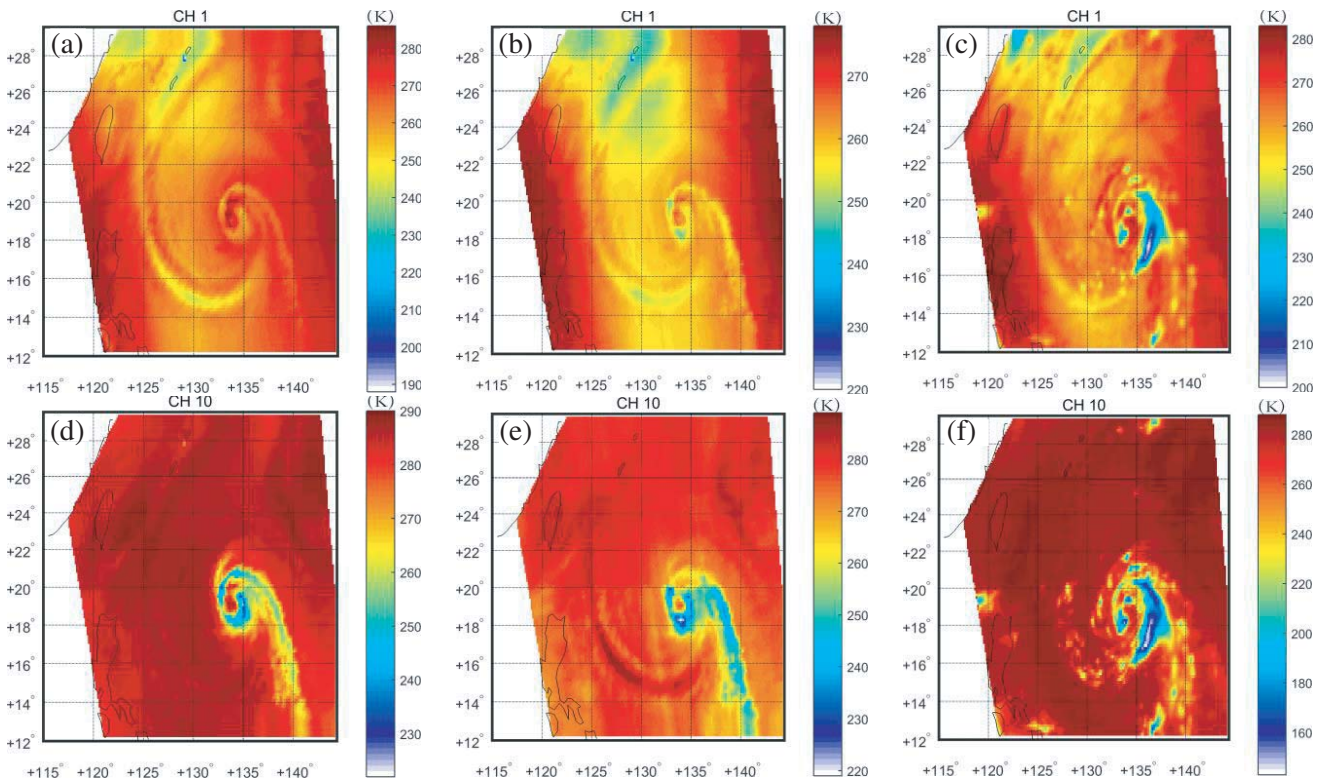


**Figure 7.** Comparison between simulated, corrected and observed TBs of the Channel 1 and 10 on 24 September 2016, at 1218 to 1400 UTC (The $x$-axis in all figures represents longitude and the $y$-axis represents latitude). (a), (d) simulated TBs; (b), (e) corrected TBs; (c), (f) observed TBs.

Figures 4–6 show that the corrected TBs are improved compared to the uncorrected TBs (simulated TBs). This is also included in Figures 7(b) and (e), which show more TC details than Figures 7(a) and (d). For the corrected TBs maps shown in Figures 7(b) and (e), TC structures and details can be seen from the two window channels. However, the outline and structure of the TC drawn using the corrected TBs are not as sharp as Figures 7(c) and (f) with the observed TBs. There are some deviations between the corrected TBs and observed TBs, mainly due to three reasons: (a) During our data matching work, there is a difference in time and space between the observed TBs and the simulated TBs. This difference will bring about some deviations in our experiments; (b) In addition, physical processes in the natural atmosphere are complicated due to various factors such as moisture, temperature, atmospheric motion, and circulation. The physical process established in the WRF model is not as accurate as the natural atmosphere; (c) The limitations of the water particle scattering module and the surface emission module in the RTTOV model also bring a very large error.

The current observation of TCs using microwave sounder makes it impossible to obtain continuous observations. Although the methods used in this paper have some limitations, which cause a certain error, it is of great significance for the continuous monitoring application and research in TCs area.

## 4.2. Precipitation Detection

Determining scattering index threshold ($SI_0$) is the key to detecting precipitation in TCs area. Before detecting precipitation area, the first thing that needs to do is to determine threshold $SI_0$, which is utilized to detect precipitation. The scattering index ($SI$) is computed according to formula (3) using the corrected TBs, and the precipitation is determined according to the comparison between $SI$ and different $SI_0$ in the range of $-50$ and 150. When $SI_0$ is ranged from $-50$ to 150, the correct percentage of detected precipitation is also changed with $SI_0$. Finally, this result is compared with the FY-3C L2 and TRMM Multi-Satellite Precipitation Analysis (TMPA) [36–38] data, respectively. Before comparing the results with TMPA data, the FY-3C MWHTS and TMPA data are matched in time and space. The matching threshold is 0.25° for latitude and longitude, and 90 minutes for time. Therefore, each FOV of the MWHTS can be matched to the corresponding TMPA data. In other words, the amount of matched data is the same as the amount of MWHTS data, as shown in the last column of Table 2.

The correct percentage results of detected precipitation are presented in Figure 8. As can be observed in Figure 8(b), when the $SI$ ranges from $-50$ to 0, the correct percentage is almost unchanged and is approximately 2% stable. When $SI$ ranges from 19 to 150, the correct percentage gradually decreases and changes slowly. However, when $SI$ ranges from 0 to 19, the correct percentage increases sharply. When $SI$ is taken as 19, the correct percentage is the highest, which is 84.35%. Therefore, $SI_0$ is found to be 19 compared with the TMPA data. Similarly, as can be observed in Figure 8(a), when $SI_0$ is taken as 16, the correct rate is as high as 83.18% compared to the FY3C MWHTS Level 2 data.

In this paper, the POD, FAR and CSI are used to validate and evaluate the precipitation detection algorithm. Perfect values of the three statistical metrics are 100%, 0% and 100%, respectively. This can also be seen in Table 4. Moreover, Table 5 and Table 6 list the three statistical metrics,
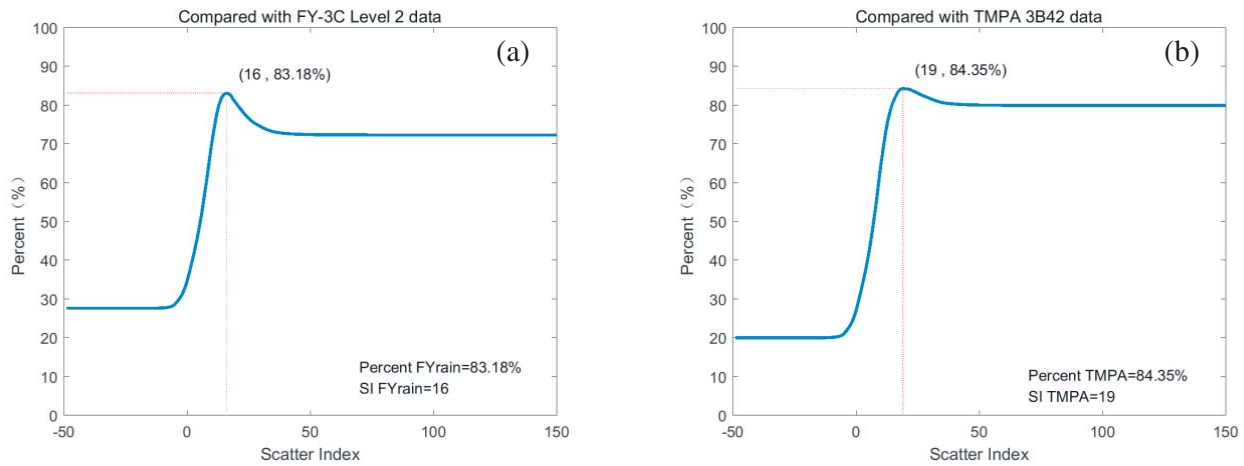


**Figure 8.** The optimal choice of scattering index threshold.

**Table 5.** Evaluation results of the precipitation detection algorithm (when $SI_0 = 16$).

| Score | FY3C MWHTS | TMPA |
|-------|------------|------|
| POD | 92.82% | 96.56% |
| FAR | 3.76% | 7.72% |
| CSI | 89.57% | 89.35% |

POD, FAR and CSI, which are used in evaluation and comparison between precipitation detection retrievals, precipitation detection products from the TMPA and FY-3C MWHTS in the TC area on 24 September 2016, at 1218 to 1400 UTC. When scattering index threshold $SI_0$ is determined to be 16, compared with the FY-3C MWHTS precipitation detection product, the POD, FAR and CSI reach 92.82%, 3.76%, and 89.57%, respectively. At the same time, compared with TMPA precipitation

**Table 6.** Evaluation results of the precipitation detection algorithm (when $SI_0 = 19$).

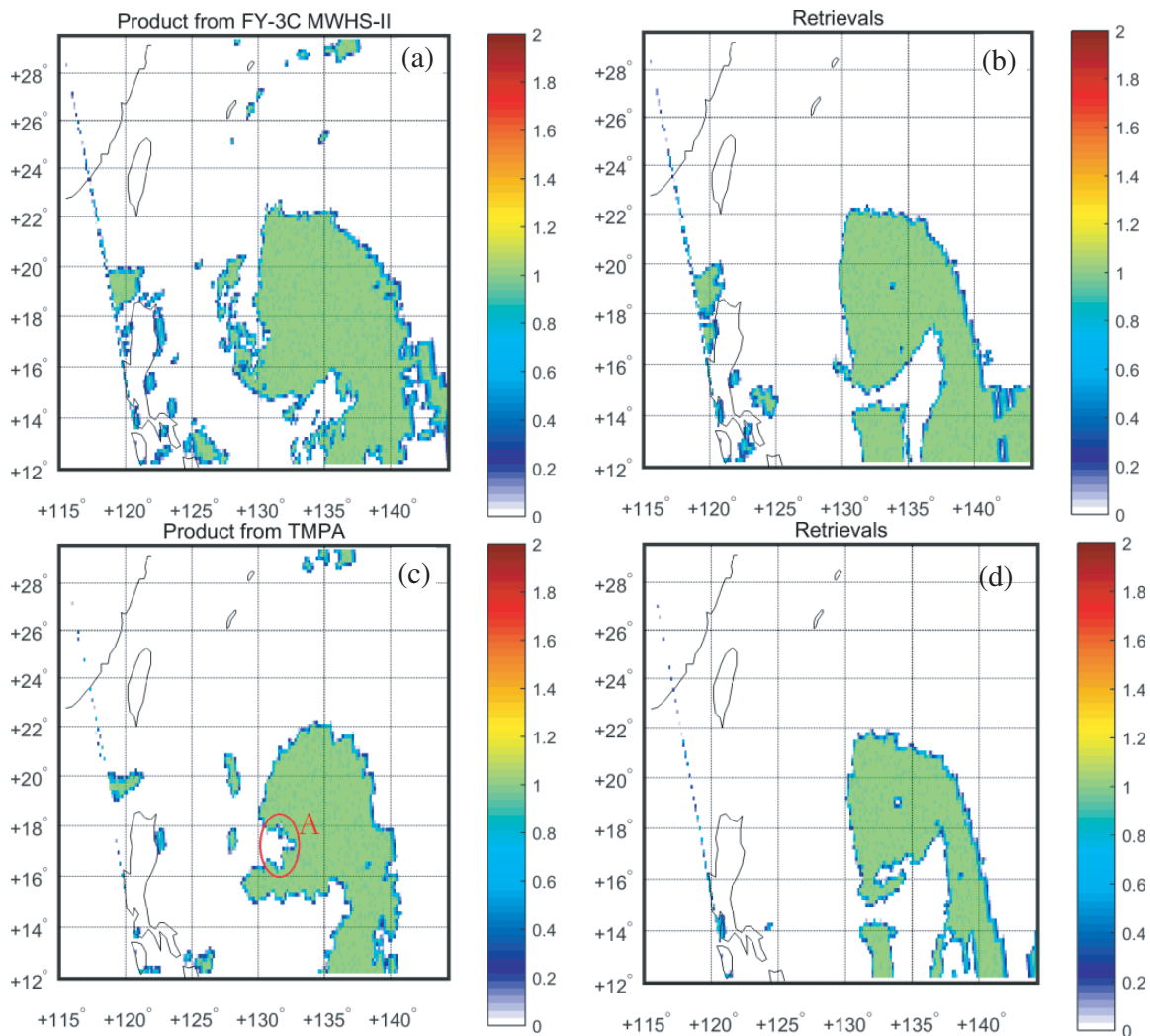| Score | FY3C MWHTS | TMPA |
|-------|-----------|--------|
| POD | 88.26% | 94.01% |
| FAR | 1.25% | 3.22% |
| CSI | 87.28% | 91.16% |



**Figure 9.** Comparison between precipitation detection retrieval, precipitation detection products from the TMPA and FY-3C MWHTS in the TC on 24 September 2016, at 1218 to 1400 UTC. (a) product from the FY-3C MWHTS; (b) retrieval (when $SI_0 = 16$); (c) product from the TMPA; (d) retrieval (when $SI_0 = 19$).

product, these three metrics reach 96.56%, 7.72%, and 89.35%, respectively. It can be seen that the POD is above 92% compared with the TMPA and FY-3C MWHTS precipitation products, which show that our precipitation detection algorithm has reached better indicators. In detail, compared with the TMPA, the POD is larger than the FY-3C MWHTS. However, the metric of FAR compared with the FY-3C MWHTS is less than the TMPA, which shows the opposite result. Additionally, compared with these two precipitation products, the CSI indicator shows little difference. When $SI_0 = 19$, the consequences of the two statistical metrics POD and FAR are similar to those at $SI_0 = 16$. However, compared with the TMPA, the CSI is larger than the FY-3C MWHTS.

The precipitation detection results in the TC area are shown in Figure 9, involving the precipitation detection retrieval and precipitation detection products from the TMPA and the FY-3C MWHTS. When the scattering index threshold is configured on 16, as expected, the determined precipitation area is greater than the scattering index threshold set to 19. In addition, the precipitation area in the retrieval precipitation map in Figure 9(b) is less than the FY-3C MWHTS products, and the banding structure of the TC cannot be observed. However, the center of the TC can be observed in Figure 9(b). Similar results are seen in Figure 9(d). These results show that the precipitation detection algorithm proposed in this paper is effective to detect the TCs precipitation center, but the algorithm cannot detect the detailed precipitation spiral rain-bands structure in the TCs.

In Figure 9(c), the elliptical area A marked with red is the non-precipitation area, but Figures 9(a), (b) and (d) show that there is the precipitation area. There are two different results for the two data products, indicating that it is difficult to ascertain the precipitation area in TCs area. At the same time, this result also demonstrates that a more accurate dataset is important to determine the precipitation area.

## 5. CONCLUSIONS

In this study, a method to simulate and correct the TBs is shown and implemented for TCs in the western Pacific. In addition, a precipitation detection algorithm is proposed to detect precipitation in TCs area.

The NCEP FNL/WRF/RTTOV method is used to simulate the TBs of the FY-3C MWHTS. After simulating TBs using the WRF and RTTOV model, simulated TBs are linearly corrected based on the field-of-views (FOVs), channels and latitude bands. Then we analyze the correction effect. The corrected TBs have less bias and root mean square error than the uncorrected TBs for all channels of the microwave sounder. In detail, the biases of all channels are within 2 K and close to zero, and the RMSEs of all channels except that Channels 10 and 15 are less than 10-K. The results show that all channels are improved after the correction. Some maps can be drawn from the corrected TBs, and the structures and position information of the TC can be clearly observed in these maps. Thus, this method makes it possible for satellite-borne sensors to continuously monitor TCs, and it can be utilized to monitor TCs with an encouraging degree of accuracy. Therefore, we expect that this method will be followed in other TCs in the Western Pacific.

In addition, we propose a calculation method for the scattering index and use the corrected TBs to detect the precipitation. 16 and 19 are adopted as the scattering index threshold to determine precipitation. The correct percentage of detected precipitation can reach 96.56%. The precipitation detection algorithm is clearly illustrated by some good indicators and can pave the way for subsequent precipitation rate retrieval and other research.

## REFERENCES

1. Available online: https://en.wikipedia.org/wiki/Tropical_cyclone (accessed on Oct. 9, 2018).

2. Mitchell, T., D. Guha-Sapir, J. Hall, E. Lovell, R. Muir-Wood, A. Norris, L. Scott, and P. Wallemacq, "Setting, measuring and monitoring targets for reducing disaster risk," *Recommendations for Post-2015 International Policy Frameworks*, ODI, 2014.

3. Zhang, Y., H. Liu, J. Wu, J. He, and C. Zhang, "In target brightness temperature simulation and analysis for the geostationary interferometric microwave sounder (GIMS)," *2015 IEEE International Geoscience and Remote Sensing Symposium (IGARSS)*, 3477–3480, IEEE, 2015.

4. Zhang, Y., H. Liu, J. Wu, C. Zhang, and J. He, "In analysis and simulation of GIMS observation on dynamic targets," *2016 IEEE International Geoscience and Remote Sensing Symposium (IGARSS)*, 426–429, IEEE, 2016.

5. Camps, A., H. Park, J. Bandeiras, J. Barbosa, A. Sousa, S. d'Addio, and M. Martin-Neira, "Microwave imaging radiometers by aperture synthesis — Performance simulator (Part 1): Radiative transfer module," *Journal of Imaging*, Vol. 2, 17, 2016.

6. He, J., S. Zhang, and Z. Wang, "Advanced microwave atmospheric sounder (AMAS) channel specifications and T/V calibration results on FY-3C satellite," *IEEE Transactions on Geoscience and Remote Sensing*, Vol. 53, 481–493, 2015.

7. Zhang, S., J. Li, Z. Wang, H. Wang, M. Sun, J. Jiang, and J. He, "In design of the second generation microwave humidity sounder (MWHS-II) for chinese meteorological satellite FY-3," *2012 IEEE International Geoscience and Remote Sensing Symposium (IGARSS)*, 4672–4675, IEEE, 2012.

8. Li, N., J. He, S. Zhang, and N. Lu, "In rainfall retrievals using 118 GHz and 183 GHz channels of MWHS-II on FY-3C meteorological satellite," *2017 IEEE International Geoscience and Remote Sensing Symposium (IGARSS)*, 4505–4508, IEEE, 2017.

9. Chen, Y., F. Weng, Y. Han, and Q. Liu, "Validation of the community radiative transfer model by using cloudsat data," *Journal of Geophysical Research: Atmospheres*, 113, 2008.

10. Han, Y., P. van Delst, F. Weng, Q. Liu, D. Groff, B. Yan, Y. Chen, and R. Vogel, "In an overview on the JCSDA community radiative transfer model (CRTM) Version 2," *Proc. 6th Annu. Symp. Future Nat. Oper. Environ. Satellite Syst.-NPOESS GOES-R*, 2010.

11. Van Delst, P., *Crtm: V2. 0 User Guide. Joint Center for Satellite Data Assimilation*, Camp Springs, Maryland, USA, 2011.

12. Ritchie, E. A. and G. J. Holland, "Large-scale patterns associated with tropical cyclogenesis in the western pacific," *Monthly Weather Review*, Vol. 127, 2027–2043, 1999.

13. Available online: http://weather.unisys.com/hurricanes/search (accessed on Oct. 9, 2018).

14. Available online: https://rda.ucar.edu/datasets/ds083.2/ (accessed on Oct. 9, 2018).

15. Zhao, T., C. Fu, Z. Ke, and W. Guo, "Global atmosphere reanalysis datasets: Current status and recent advances," *Advances in Earth Science*, Vol. 3, 2, 2010.

16. Skamarock, W. C., "A description of the advanced research WRF Version 3," Tech. Note, 1–96, 2008.

17. Skamarock, W. C. and J. B. Klemp, "A time-split nonhydrostatic atmospheric model for weather research and forecasting applications," *Journal of Computational Physics*, Vol. 227, 3465–3485, 2008.

18. Available online: http://www2.mmm.ucar.edu/wrf/users/ (accessed on Oct. 9, 2018).

19. Hocking, J., P. Rayer, D. Rundle, R. Saunders, M. Matricardi, A. Geer, P. Brunel, and J. Vidot, *Rttov v11 Users Guide*, Met Office, Exeter, UK; ECMWF; Météo, France, 2015.

20. Zou, X., X. Wang, F. Weng, and G. Li, "Assessments of Chinese Fengyun microwave temperature sounder (MWTS) measurements for weather and climate applications," *Journal of Atmospheric and Oceanic Technology*, Vol. 28, 1206–1227, 2011.

21. Hong, S.-Y. and J.-O. J. Lim, "The WRF single-moment 6-class microphysics scheme (WSM6)," *J. Korean Meteor. Soc.*, Vol. 42, 129–151, 2006.

22. Kain, J. S., "The Kain-Fritsch convective parameterization: An update," *Journal of Applied Meteorology*, Vol. 43, 170–181, 2004.

23. Dudhia, J., "Numerical study of convection observed during the winter monsoon experiment using a mesoscale two-dimensional model," *Journal of the Atmospheric Sciences*, Vol. 46, 3077–3107, 1989.

24. Mlawer, E. J., S. J. Taubman, P. D. Brown, M. J. Iacono, and S. A. Clough, "Radiative transfer for inhomogeneous atmospheres: RRTM, a validated correlated-k model for the longwave." *Journal of Geophysical Research: Atmospheres*, Vol. 102, 16663–16682, 1997.

25. Chen, F. and J. Dudhia, "Coupling an advanced land surface — hydrology model with the penn state — NCAR MM5 modeling system. Part I: Model implementation and sensitivity," *Monthly Weather Review*, Vol. 129, 569–585, 2001.

26. Tewari, M., F. Chen, W. Wang, J. Dudhia, M. LeMone, K. Mitchell, M. Ek, G. Gayno, J. Wegiel, and R. Cuenca, "Implementation and verification of the unified noah land surface model in the WRF model," *20th Conference on Weather Analysis and Forecasting/16th Conference on Numerical Weather Prediction*, 2004.

27. Hong, S.-Y., Y. Noh, and J. Dudhia, "A new vertical diffusion package with an explicit treatment of entrainment processes," *Monthly Weather Review*, Vol. 134, 2318–2341, 2006.

28. Shimadera, H., A. Kondo, K. L. Shrestha, K. Kitaoka, and Y. Inoue, "Numerical evaluation of the impact of urbanization on summertime precipitation in Osaka, Japan," *Advances in Meteorology*, 2015.

29. Harris, B. and G. Kelly, "A satellite radiance-bias correction scheme for data assimilation," *Quarterly Journal of the Royal Meteorological Society*, Vol. 127, 1453–1468, 2001.

30. Wilheit, T., C. D. Kummerow, and R. Ferraro, "Nasdarainfall algorithms for AMSR-E," *IEEE Transactions on Geoscience and Remote Sensing*, Vol. 41, 204–214, 2003.

31. Grody, N. C., "Classification of snow cover and precipitation using the special sensor microwave imager," *Journal of Geophysical Research: Atmospheres*, Vol. 96, 7423–7435, 1991.

32. Li, N., J. He, S. Zhang, and N. Lu, "Global precipitation detection based on MWHS-II from China FY-3C meteorological satellite," *2018 IEEE International Geoscience and Remote Sensing Symposium (IGARSS)*, 923–926, IEEE, 2018.

33. Behrangi, A., Y. Tian, B. H. Lambrigtsen, and G. L. Stephens, "What does cloudsat reveal about global land precipitation detection by other spaceborne sensors?," *Water Resources Research*, Vol. 50, 4893–4905, 2014.

34. Wang, W., H. Lu, T. Zhao, L. Jiang, and J. Shi, "Evaluation and comparison of daily rainfall from latest GPM and TRMM products over the mekong river basin," *IEEE Journal of Selected Topics in Applied Earth Observations and Remote Sensing*, Vol. 10, 2540–2549, 2017.

35. Yamamoto, M. K., I. Tanaka, and S. Shige, "Improvement of the rain/no-rain classification method for microwave radiometers over the tibetan plateau," *IEEE Geoscience and Remote Sensing Letters*, Vol. 14, 626–630, 2017.

36. Scheel, M., M. Rohrer, C. Huggel, D. S. Villar, E. Silvestre, and G. Huffman, "Evaluation of trmm multi-satellite precipitation analysis (TMPA) performance in the central andes region and its dependency on spatial and temporal resolution," *Hydrology and Earth System Sciences*, Vol. 15, 2649–2663, 2011.

37. Ochoa, A., L. Pineda, P. Crespo, and P. Willems, "Evaluation of trmm 3b42 precipitation estimates and wrf retrospective precipitation simulation over the Pacific-Andean region of ecuador and peru," *Hydrology and Earth System Sciences*, Vol. 18, 3179–3193, 2014.

38. Chen, S., Y. Hong, Q. Cao, J. J. Gourley, P. E. Kirstetter, B. Yong, Y. Tian, Z. Zhang, Y. Shen, and J. Hu, "Similarity and difference of the two successive v6 and v7 TRMM multisatellite precipitation analysis performance over china," *Journal of Geophysical Research: Atmospheres*, Vol. 118, 13060–13074, 2013.